Improvement of the Arcan setup for the investigation of thin sheet behavior under shear loading

A Zaplatić, Z Tomičević, D Čakmak, François Hild

Experimental Mechanics manuscript No.
(will be inserted by the editor)

Improvement of the Arcan setup for the investigation of thin sheet behavior under shear loading

A. Zaplatić · Z. Tomičević · D. Čakmak · F. Hild

Received: date / Accepted: date

Abstract Background: Accurate predictions of thin sheet material springback during forming processes are of great interest in the forming industry. However, thin sheets are susceptible to buckling under shear loading. Objective: The present research aims at improving the so-called Arcan setup for testing thin (1-5 mm) sheet samples with large gauge areas (*i.e.,* width about 21 mm) by introducing anti-buckling devices to mitigate sample buckling. Method: Three monotonic and one cyclic shear tests were carried out on 1 mm thick C60 high carbon steel. Results: The use of the proposed anti-buckling device resulted in the suppression of sample buckling. Numerical analyses of the experiment where buckling was eliminated revealed predominant shear stress states in the gauge area (*i.e.,* stress triaxiality =

A. Zaplatić, Z. Tomičević*, D. Čakmak

University of Zagreb, Faculty of Mechanical Engineering and Naval Architecture, Ivana Lučića 5, 10002 Zagreb, Croatia

*Corresponding author. Email: zvonimir.tomicevic@fsb.hr

F. Hild

Université Paris-Saclay, ENS Paris-Saclay, CNRS

LMT - Laboratoire de Mécanique et Technologie, 91190 Gif-sur-Yvette, France

0), which highlights minor influences of the anti-buckling device on the sample stress state. Conclusion: To suppress buckling, the use of anti-buckling devices was essential. Moreover, the friction coefficient between the sample and the proposed devices was calibrated ($\mu = 0.33$) in addition to kinematic hardening parameters.

Keywords Arcan fixture · Buckling · Simple shear · Stereocorrelation · Thin sheet

1 Introduction

The growing demand for light-weight engineering components of high quality requires equally fast and adaptive production processes in order to meet the demand-supply balance. As a result, at the end of the 20-th century, the implementation of numerical simulations and modeling of sheet metal forming processes gained traction. The role of numerical simulations was to predict material flow, to analyze stress-strain relationships, and to improve the quality of manufactured components [1]. Expensive and time consuming trial and error methods for analyzing production processes had to be minimized. For instance, industries involving metal forming relied on numerical simulations of manufacturing processes where shear is an important stress state [2]. Since pure shear cannot be obtained experimentally, mechanical tests involving simple shear are often carried out on thin sheets.

Simple shear tests provide a comprehensive characterization of the anisotropy of flat samples experiencing large strains [3, 4, 5]. Since the sample geometry is essential in understanding the material response due to simple shear, many authors have proposed different approaches to their design. Furthermore, the sample geometry directly determines which material property is sought (*e.g.,* elasto-plasticity [6, 4], shear fracture [7, 8]). The design of samples should possibly provide homogeneous shear stress states in the gauge area.

Miyauchi [6] proposed a complex geometry containing three clamped bars linked by the two sheared zones (*i.e.,* gauge areas). By pulling the central bar, shear stress states were induced in the gauge areas. The sample geometry according to ASTM B831 standard [9] contains two slant slits, thereby establishing a single shear zone in the middle of the sample. Merklein and Biasutti [10] modified the ASTM geometry to enable for compressive loadings. A comprehensive study carried out by Yin *et al.* [11], where the aforementioned geometries were compared, yielded good agreement for the shear stress vs. strain responses for each investigated test.

Peirs *et al.* [7] developed a flat shear sample, which was based upon the geometry proposed by Bao *et al.*[12], with asymmetric rounded off notches with eccentricity that promoted shear stress states in the gauge area (*i.e.,* stress triaxiality close to zero). Reyes *et al.* [13] optimized the geometry containing two slant slits with respect to stress homogeneity and triaxiality for static and dynamic shear experiments. The geometry of the slits was changed to a semi-circular shape with V notches to promote uniform strain distributions. Roth and Mohr [14] carried out a comprehensive study of Peirs' shear sample to obtain reliable shear strain measurements at fracture. As a result, three modified geometries were proposed for various levels of material ductility. Furthermore, Roth and Mohr [15, 8] optimized the so-called *smiley* geometry with two parallel gauge sections for in plane shear testing by modifying the notch geometry to avoid premature fracture initiation near the free gauge boundaries. To prevent buckling of the sample, the width and height of the gauge section were of the same order of magnitude as the thickness.

Iosipescu [16] proposed a flat sample geometry with two symmetric V notches (*i.e.,* butterfly sample) in the gauge region to induce quasi uniform shear states between V notches. Mohr and Henn [17] designed butterfly specimens with thickness reduction in the gauge area for investigating the fracture of metallic materials in a wide range of triaxialities. Moreover,

Mohr and Oswald [18] improved the biaxial testing machine developed by Mohr and Doyoyo [19], which was based on the Arcan fixture [20]. It enabled the authors to investigate the material behavior with the aforementioned butterfly sample under combined tensile and shear loadings. Further improvements to the sample geometry [21] were proposed for investigating fracture under combined normal and shear stresses. Abedini *et al.* [22, 23] analyzed the influence of two sample geometries (*i.e.,* Peirs' mini-shear sample [7] and the butterfly geometry [21]) on the fracture of thin sheets. The butterfly sample achieved lower fracture strains than its counterpart. However, it was deemed useful for quasi-static fracture characterization in shear and plane strain/stress states. Furthermore, Peshekhodov *et al.* [24] developed a butterfly sample for fracture characterization of advanced high strength steel sheets under shear, tensile and combined stress states.

The aim of this research is to discuss a modified Arcan setup to investigate the behavior of butterfly specimens made of 1 mm C60 high carbon steel. The thin sheet samples were designed with *large* gauge areas (*i.e.,* height equal to 21 mm), whereas the previously discussed shear geometries contained small gauge zones (*i.e.,* < 3 mm). The latter ones were designed to promote uniform shear stress states and to reduce buckling [25, 4, 26]. However, samples with large gauge areas are prone to buckling due to increased width to thickness ratios. Buckling restricts the use of standard optical measurement methods for determining the material response under simple shear loading. Therefore, to prevent buckling, transparent anti-buckling devices made of acrylic glass were added. Three monotonic and one cyclic shear tests were carried out and monitored with a stereovision system. Furthermore, the influence of the anti-buckling device was evaluated numerically by observing the contribution of friction to the calibrated plasticity parameters via Finite Element Model Updating (FEMU) [27] and to stress triaxiality fields. Last, friction was calibrated in addition to the kinematic hardening parameters of the investigated steel.

2 Modified Arcan fixture and tested samples

In this section, the modifications to the Arcan fixture are presented. They include increased thickness of the fixture, upgraded gripping system of the tested samples, and modular design of the fixture. Additionally, changes to the butterfly geometry are also presented.

2.1 Modified Arcan device

The Arcan fixture [20] was designed as two separate semi-circular symmetrical plates made of aluminum alloy. The butterfly samples were glued to the supporting plates, and subjected to in-plane shear loadings. For the present study, the Modified Arcan Fixture (MAF, see Figure 1) was designed to study the mechanical response of thin (*i.e.,* $\leq$ 5 mm in thickness) metal sheets subjected to in-plane tensile, simple shear and combined loadings with expected triaxiality values of 0.33, 0 and < 0.66 in the gauge areas, respectively. The main advantage of the MAF is an increased stiffness of the fixture to avoid out-of-plane bending, and a modular design to allow for varying sample thicknesses. Figure 1 shows the MAF that consists of two separate yet identical semi-circular 35-mm thick supporting plates (*i.e.,* rigs), two sets of gripping jaws, and two identical testing machine adapters.

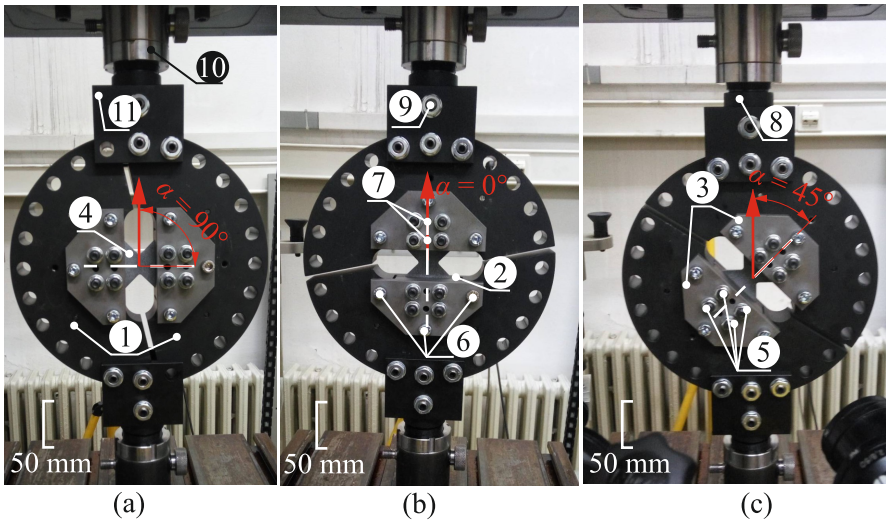

Fig. 1: Loading configurations of the Modified Arcan Fixture. (a) Simple shear configuration, (b) tensile loading configuration, and (c) combined shear/tensile loading configuration. See text for the description of the labels

The Arcan rig (1) (Figure 1) is made of M200 steel plates with a radius of 123.5 mm. The use of high strength steel (*i.e.,* $\sigma_y = 1000$ MPa) ensures that the fixture does not enter the plastic regime during tests. Near the peripheral area of the rigs, a series of twelve 13-mm in diameter holes was drilled $15°$ apart. The prescribed load onto the butterfly sample is selected by the loading holes. For example, pure tension ($\alpha = 0°$), simple shear ($\alpha = 90°$) and combined loadings ($0° < \alpha < 90°$) can be applied. The front central part of the rigs contains milled rectangular openings designed to hold the gripping jaws and the butterfly sample. The size of the rectangular openings is 75×35 mm with a depth of 25 mm from the front face. The rectangular openings result in asymmetric distributions of rig stiffness (*i.e.,* the rear side of the fixture is stiffer than the front side). This shortcoming manifested itself in the form of out-of-plane bending of the sample since the load distribution induced

spurious bending. The aforementioned imperfection was compensated with the appropriate design of the gripping jaws (2) and (3) (Figure 1).

The gripping jaw (2) serves as a placeholder to prevent any motion of the sample. The jaw (3) was designed with dual purpose. The primary purpose is to connect the sample (4) to the fixture via two sets of four M8 bolts (5). The secondary role is to increase the rigidity of the front side of the rigs, which is established by directly connecting jaw (3) to the front side via three additional M8 bolts (6). As a result, the rigs and griping jaws behave as a single solid part. Two additional pins (7) were added to prevent bolt shearing. Moreover, the gripping system was designed to ensure the coaxiality between the loading axis and that of the sample. To prevent slip of the sample, the contact surfaces on the gripping jaws were knurled.

The connection between the fixture and the testing machine is established via two adapters (8). They consist of a central shaft, which is fastened to the testing machine via a single 13-mm in diameter pin (9), the lock nut (10), and two tabs (11) on the sides of the shaft. Each tab consists of three loading holes equally spaced according to the layout on the rigs. The central shaft of the Arcan adapter was designed with a radius less than the machine connector slot. As a result, a clearance is present between the Arcan adapter and the machine slot. Since the Arcan fixture is connected to the machine with a single pin, a single rotational degree of freedom is allowed. During tests, the fixture has the ability for self-alignment. However, to compensate for the aforementioned clearance, the Arcan adapter was also threaded at the connection point with the machine. This modification allows for the use of lock nut (10). By tightening the nut, the adapter is firmly pushed into the connector slot of the machine, thereby increasing the preload on the sample.

2.2 Butterfly sample

The butterfly sample (Figure 2) was designed with two symmetric V notches for localizing the plastic strains in the narrow gauge area (*i.e.,* between the two V notches). The surface of the sample is divided into three regions, namely, the gripped area, the observable area during tests and the Region of Interest (ROI) for stereocorrelation analyses. The dimensions of the gripped area, shown as red hatched in Figure 2(a), correspond to those of the contact surfaces of gripping jaws (2) and (3). Since the gripped surfaces cannot be monitored during tests, only a 30×40-mm^2 surface area is visible. However, the chosen ROI, depicted by green hatches, was smaller than the observable area of the sample. This choice is justified by the fact that shear strains were concentrated in the gauge area close to the ligament.

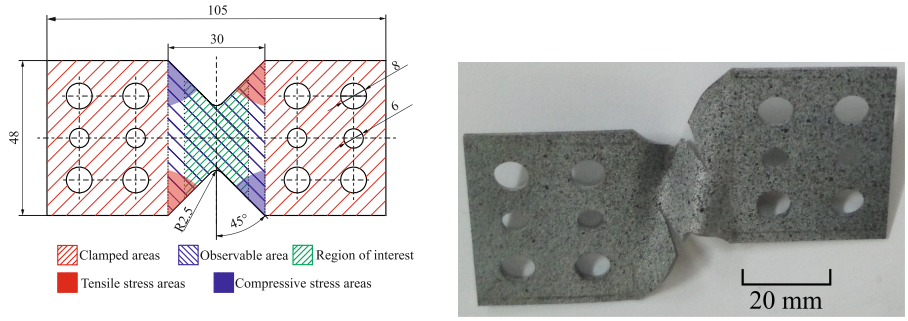

Fig. 2: (a) Butterfly geometry with characteristic regions (see text). The various stress areas are depicted for simple shear loading. Dimensions are in mm. (b) Buckled E1 sample under simple shear loading in the modified Arcan fixture

On each end of the sample, four 8-mm holes were drilled to allow the threaded M8 bolts to pass through to tighten the sample and the fixture together. Tightening the sample with

four bolts makes the contact pressure more uniform. Two additional holes for 6-mm pins were added to prevent bolt shearing.

3 Experimental investigation

The experimental investigation presented herein was performed with the MAF. The latter offers three main loading modes depending on the angle α of the fixture with respect to the loading axis of the testing machine (depicted by the red arrow in Figure 1). The first loading configuration (Figure 1(a)) induces simple shear stress states in the gauge area of the sample, whereas the second loading configuration (Figure 1(b)) corresponds to tensile loading where the expected triaxiality levels in the gauge area are around 0 and 0.33, respectively. Furthermore, the combination of both loading configurations (Figure 1(c)) enables for the application of combined shear/tensile loadings with expected triaxialities in the gauge area ranging from 0 to 0.66.

3.1 Buckling under shear loading

The accurate characterization of thin sheets subjected to shear loading is challenging [25, 4, 26]. The samples are generally thin with a large gauge width to thickness ratio inducing folding of the sample (Figure 2(b)). Saurupt et al. [25] concluded that the folding mechanism could be interpreted as buckling due to compressive stresses. Due to sample clamping, the material close to two diagonally opposed corners of the unclamped region is subjected to tension while the other corners are subjected to compression. Where compression occurs, buckling initiation was reported [4]. Such mechanism may be prevented using additional supports placed on the observed region of interest [28], or by changing the sample gauge width [4].

The butterfly sample subjected to shear loading on the MAF exhibited buckling. This phenomenon was observed for sample thicknesses less than 2 mm (Figure 2(b)). In the experimental investigations presented herein, the behavior of 1-mm thick butterfly samples, made of C60 high carbon steel, was sought. Therefore, in order to suppress the initiation of buckling, additional supports in the form of two transparent plates made of Poly methyl methacrylate (PMMA) were selected. Such configuration was already used to successfully mitigate wrinkling in 1D and 2D tests on sub-millimeter sheets [29, 30]. The dimensions of the PMMA plates (*i.e.,* 70×25 mm) were chosen with respect to the observable area (Figure 2(a)). Moreover, the transparency of PMMA allows optical measurement methods to be employed. Stereocorrelation was applied to measure displacement and strain fields of the ROI. The application of the supports is straightforward. Each plate was placed on the front and back surfaces of the sample and was connected via six M5 bolts.

3.2 Experimental setup

In order to determine the influence of the additional support on the mitigation of buckling, an appropriate experimental protocol had to be defined. The three configurations employed in this investigation are presented in Table 1. Furthermore, the influence of the stiffness of the connection between the MAF and the testing machine had to be studied. Pham et al [28] determined that clamping of the fixture (*i.e.,* increasing the stiffness of the fixture) resulted in stress perturbations in the sample, thereby leading to buckling initiation. Higher stiffnesses of the MAF are achieved by tightening the lock nut on the testing machine adapter. Consequently, additional tensile/compressive preloads could be applied to the tested samples.

Table 1: Experimental configurations (M: monotonic, C: cyclic)

Test	E1	E2	E3	E4
Configuration	#1	#2	#3	#3
Loading regime	M	M	M	C
Thickness of PMMA plates, mm	–	5	10	10
Preload, N	-39	-1000	-40	-35

The first configuration was characterized by a loosened connection between the MAF and the testing machine. Furthermore, no additional support was applied. However, even with the allowed self-alignment of the MAF, buckling of the sample occurred (Figure 2(b)). Therefore, in the second configuration, an additional support with 5-mm thick PMMA plates was employed. Higher stiffness of the MAF was achieved and the measured preload was equal to -1000 N (Table 1). Although the PMMA support was applied, buckling of the sample was observed, which fractured the plates. For that reason, the third configuration employed 10-mm thick plates, and a loosened connection between the MAF and the testing machine. The third configuration suppressed buckling initiation. An additional cyclic test was then performed with the third configuration for further validation purposes.

The shear tests were carried out on a uniaxial testing machine *Messphysik Beta* 50-5 in controlled displacement with a stroke rate of 1 mm/min. The material response in the observed ROI (Figure 2) was monitored by a stereovision system. The image acquisition rate for the monotonic (*i.e.,* E1, E2 and E3) experiments was 1 fps, whereas for the cyclic (*i.e.,* E4) test it was 0.3 fps. The hardware parameters of the optical setup are listed in Table 2.

Table 2: Hardware parameters of the stereovision system

Cameras	Dalsa Falcon 4M60
Definition	2358×1728 pixels (B/W images)
Color filter	none
Gray Levels rendering	8 bits
Lens	Titanar 50 mm
Aperture	f/2.8
Field of view	3,996 mm^2
Image scale	≈ 32 pixel/mm
Stereo-angle	25°
Stand-off distance	31.6 cm
Image acquisition rate	1 fps (0.3 fps for test E3)
Patterning technique	B/W paints
Pattern feature size	15 px

The experimental investigation employing the MAF (1) (Figure 3) was monitored by the optical setup (Figure 3) consisting of two vertically positioned Dalsa cameras (2) and (3) (Figure 3) and two light sources (4). The vertical layout of the cameras was chosen in order to achieve maximum spatial resolution for the ROI. The stereovision system captured the entire gauge area of the sample (5) *and* the additional PMMA supports (6).

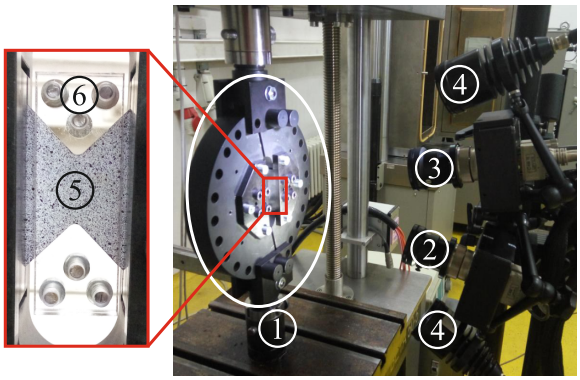

Fig. 3: Experimental and optical setups used for stereocorrelation measurements. See text for the description of the labels

For this study, FE-based stereocorrelation [31, 32, 33] was utilized for measuring displacement and strain fields in the region of interest (ROI). The aforementioned algorithm uses a continuous description of the observed surface discretized with triangular finite elements. The commercial code EikoTwin DIC [34] was used. The calibration was carried out in two steps. For the pre-calibration step, a first estimation of the projection matrix was sought for each camera. During this process, the scale factor (*i.e.,* conversion between pixel and mm) was set. An FE mesh was created, which corresponded to the nominal geometry of the sample *and* the fixture (Figure 4(a)) that were observed by both cameras. Since each camera was independent at this stage, different points were chosen for the left and right camera pictures. These points must be distributed in the entire 3D volume that is covered by each camera. A total of 8 points was chosen in two different planes and the first estimates of the projections matrices were obtained for this self-calibration route [35]. The pre-calibration step allows in particular for the verification of the reprojection of the measurement mesh (Figure 4(b)).

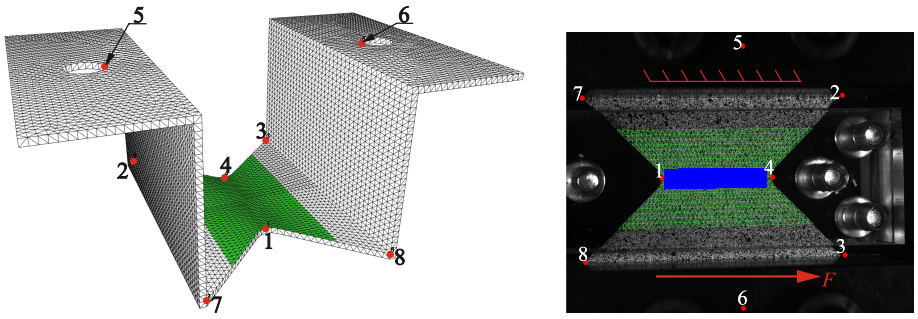

(a) (b)

Fig. 4: Chosen reference points on the FE mesh and one of the reference images for the pre-calibration step. (a) User defined points (*i.e.,* fiducials) on the FE mesh, and (b) on one of the reference pictures used in the pre-calibration step. The (green) mesh of the ROI is also shown in the 3D model and its reprojection in one of the reference pictures. The blue rectangle depicts the area over which the average strains were assessed

The calibration step was then performed to determine the best projection matrices via global registrations [35] of the two reference images based on the knowledge of the nominal geometry. It was initialized with the projection matrices determined during the pre-calibration step. Once the calibration step was carried out, shape corrections were performed for the actual ROI (Figure 4(b)) by running a second series of spatial registrations in which out-of-plane corrections were allowed [32].

Last, displacement fields were measured by performing temporal registrations in which the nodal displacements were determined [31, 36, 33]. The stereocorrelation parameters are listed in Table 3. The noise floor estimates were obtained by calculating the (temporal) standard deviations of the nodal displacements and strains from the registration of ten image pairs acquired in the unloaded states.

Table 3: Stereocorrelation analysis parameters

DIC software	EikoTwin DIC
Image filtering	none
Element length	1 mm
Shape functions	linear (T3 elements)
Mesh	see Figure 4
Matching criterion	penalized sum of squared differences
Regularization length	5 mm
Displacement noise floor for test E1 (x z y)	0.4 µm 0.2 µm 0.7 µm
Displacement noise floor for test E2 (x z y)	0.1 µm 0.2 µm 0.5 µm
Displacement noise floor for test E3 (x z y)	0.2 µm 0.1 µm 0.6 µm
Displacement noise floor for test E4 (x z y)	0.2 µm 0.2 µm 0.6 µm
Strain ϵ_{xz} noise floor for test E1	6×10^{-5}
Strain ϵ_{xz} noise floor for test E2	6×10^{-5}
Strain ϵ_{xz} noise floor for test E3	7×10^{-5}
Strain ϵ_{xz} noise floor for test E4	8×10^{-5}

Figure 5 displays the load histories of the four tests reported herein. For each test, six characteristic points were chosen for which the stereocorrelation results are discussed in the following subsections.

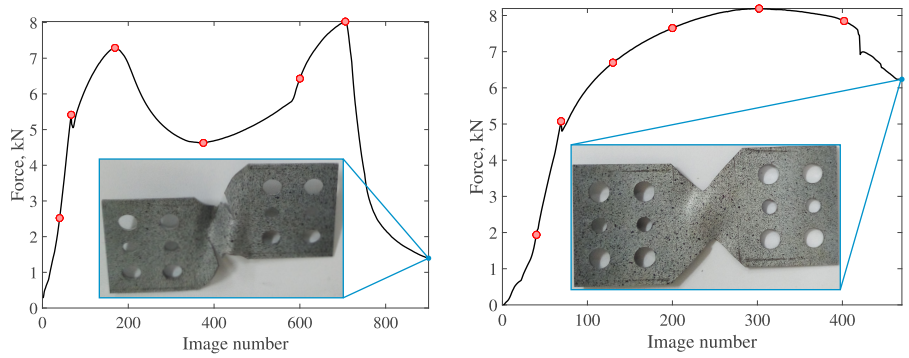

(a) E1

(b) E2

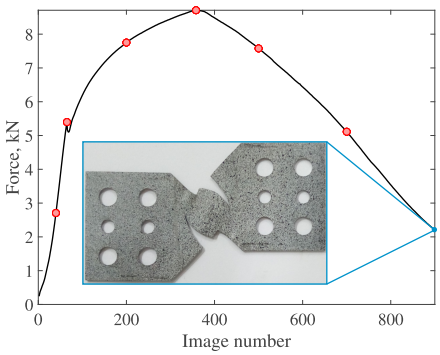

(c) E3

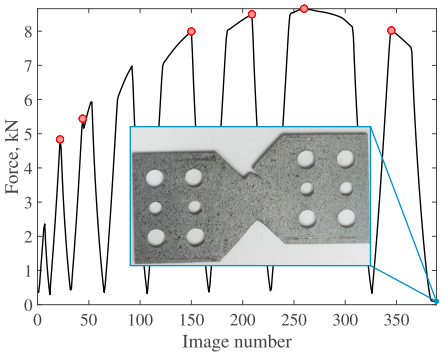

(d) E4

Fig. 5: Load histories for tests E1, E2, E3 and E4. Six characteristic points are outlined by red circles for each experiment for which the stereocorrelation results are discussed hereafter

3.3 Test E1

The loading history of test E1 (Figure 5(a)) displays a disrupted response. Since no PMMA support was utilized, buckling occurred (Figure 2(b)), thereby resulting in lower load levels. The first peak load was equal to 7.2 kN for a shear strain of 17.5%. The kinematic fields corresponding to the characteristic points shown in Figure 5(a) are reported in Appendix A.

3.4 Test E2

The loading history of test E2 shown in Figure 5(b) exhibited a more stable behavior compared to the E1 loading history (Figure 5(a)). This trend was due to the application of the 5-mm thick plates, which delayed buckling inception. However, since the stiffness of the connection between the MAF and the testing machine was high, buckling was not totally suppressed. This mechanism led to the failure of the PMMA supports and the test was interrupted. The kinematic fields corresponding to the characteristic points shown in Figure 5(b) are reported in Appendix A.

3.5 Test E3

Figure 5(c) shows the loading history of test E3. Compared to the loading histories of tests E1 (Figure 5(a)) and E2 (Figure 5(b)), the highest load level was reached in test E3. The 10-mm thick support did not fail. The connection stiffness between the MAF and the testing machine was loosened again. As a result, buckling was prevented, thus the material response could be observed more clearly.

Figure 6 displays the measured out-of-plane displacement fields for test E3. Since the 10-mm thick plates were employed, negligible amplitudes were measured throughout the experiment. This result proves that the plate thickness was sufficient to significantly lower the amplitudes of out-of-plane motions. In elasticity (Figure 6(a)) and early plasticity (Figure 6(b)), the displacements were of the same order of magnitude. Increases in magnitude observed in Figure 6(c) were due to the tendency toward buckling (as seen in test E1). However, the additional supports prevented further increases. The displacement fluctuations were attributed to buckling. Even for the highest achieved load (Figure 6(d)), the out-of-plane dis-

placements were considered negligible. However, after damage initiation and growth (Figure 6(e-f)), thinning of the sample was observed around the roots of the V notches.

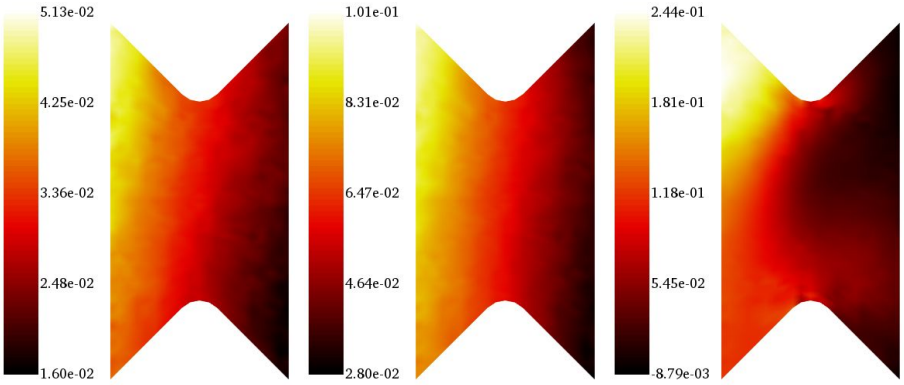

(a) $F = 2.7\text{kN}, \epsilon_{xz} = 0.12\%$ **(b)** $F = 5.4\text{kN}, \epsilon_{xz} = 0.37\%$ **(c)** $F = 7.75\text{kN}, \epsilon_{xz} = 22.7\%$

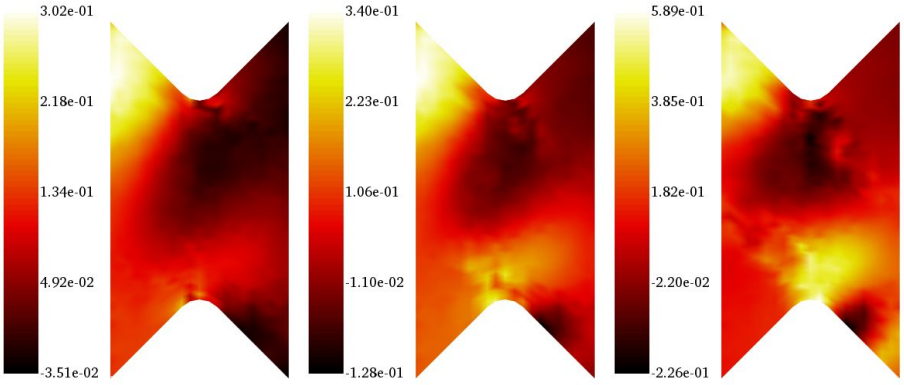

(d) $F = 8.71\text{kN}, \epsilon_{xz} = 48.7\%$ **(e)** $F = 7.6\text{kN}, \epsilon_{xz} = 70.82\%$ **(f)** $F = 5.1\text{kN}, \epsilon_{xz} = 92.2\%$

Fig. 6: Measured out-of-plane displacement fields for test E3. The displacements are expressed in mm

The analysis of the axial displacements (*i.e.,* perpendicular to the loading direction, see Figure 4(b)) revealed rotations of the ROI (Figure 7(a)). This trend also occurred in the plastic regime (Figure 7(b)). Furthermore, the axial displacements showed two emerging discontinuities, which are indicated by arrows in Figure 7(c). These “discontinuities” were

also observed in the strain (Figure 8(f)) and residual (Figure 9(c)) maps, and corresponded to two symmetrically propagating cracks.

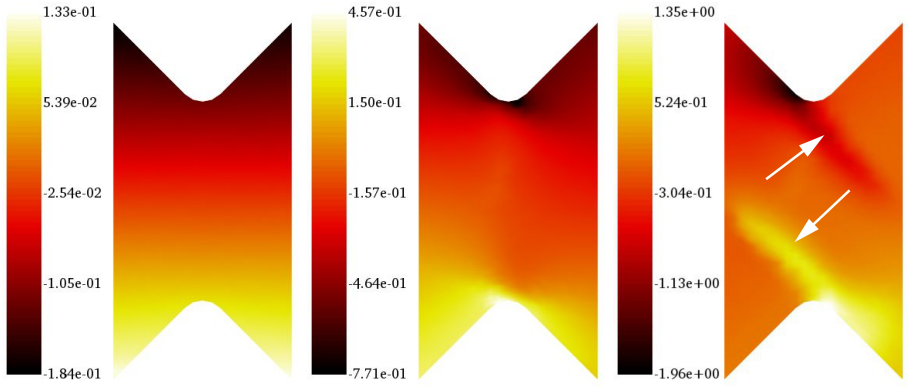

(a) $F = 5.4\text{kN}, \epsilon_{xz} = 0.37\%$ **(b)** $F = 8.71\text{kN}, \epsilon_{xz} = 48.7\%$ **(c)** $F = 5.1\text{kN}, \epsilon_{xz} = 92.2\%$

Fig. 7: Measured axial displacements for test E3. The arrows indicate the location of cracks. The displacements are expressed in mm

Figure 8 shows the measured shear strain fields. Similarly to the previous two tests, the strain distribution in elasticity (Figure 8(a)) and in the transition to plasticity (Figure 8(b)) was essentially uniform. Furthermore, the achieved strain levels were at least one order of magnitude higher than the noise floor levels (Table 3). No damage was detected in the correlation residual map (Figure 9(a)). Furthermore, a single strained band developed between the V notches (Figure 8(c)). Comparing the strain levels achieved for approximately equal loads, tests E3 (Figure 8(c)) and E2 (Figure 22(d)) led similar values, which further confirmed that no buckling occurred in test E2 at that point. Overall, larger strain levels were reached in test E3 in comparison to tests E1 and E2.

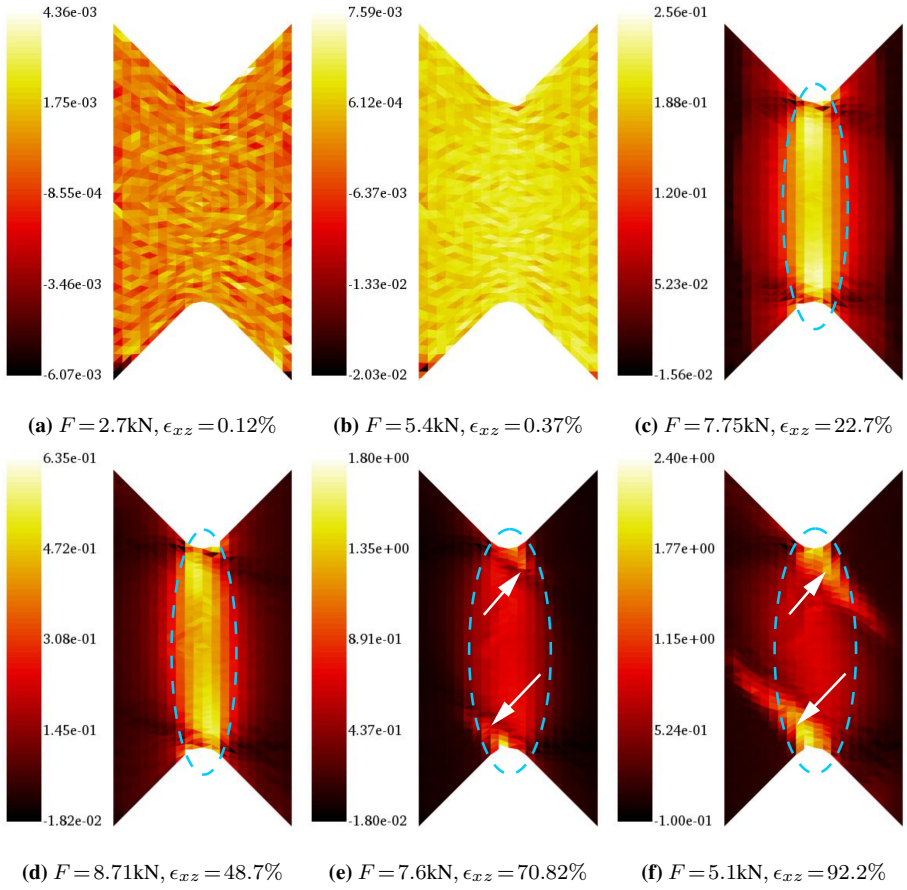

(a) $F = 2.7\text{kN}, \epsilon_{xz} = 0.12\%$ **(b)** $F = 5.4\text{kN}, \epsilon_{xz} = 0.37\%$ **(c)** $F = 7.75\text{kN}, \epsilon_{xz} = 22.7\%$

(d) $F = 8.71\text{kN}, \epsilon_{xz} = 48.7\%$ **(e)** $F = 7.6\text{kN}, \epsilon_{xz} = 70.82\%$ **(f)** $F = 5.1\text{kN}, \epsilon_{xz} = 92.2\%$

Fig. 8: Measured ϵ_{xz} strain fields for test E3. The strained band is outlined by dashed blue ellipses, whereas the location of the cracks are indicated by arrows

For the highest load level, the corresponding strain level was equal to 48.7% (Figure 8(d)). Very high gradients were observed in the strain fields (see Figures 8(e-f)), which were also present in axial displacement fields (Figure 7(c)) and correlation residual maps (Figure 9(b-c)). These "discontinuities" correspond to initiated and growing cracks. Since the sample had a tendency toward buckling, slight folding occurred in the center of the ROI, which caused changes in brightness (*i.e.,* shadows). These changes in brightness were

observed as an increase in the correlation residuals in the ROI center (Figure 9(b-c)). The correlation residuals are sensitive to damage initiation and growth [37]. Observing the correlation residual maps allowed mesocracks to be detected and quantified (*i.e.,* symmetric initiation and propagation of two cracks from each V-notch, see Figure 9(c)). Last, comparing the correlation residual maps with the final deformed shape of the sample (Figure 5(c)) shows a good agreement for the location and size of the cracks.

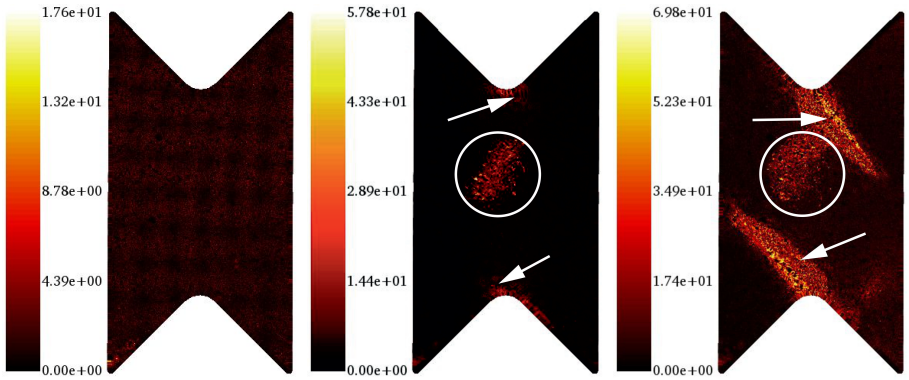

(a) $F = 5.4$kN, $\epsilon_{xz} = 0.37\%$ **(b)** $F = 8.71$kN, $\epsilon_{xz} = 48.7\%$ **(c)** $F = 5.1$kN, $\epsilon_{xz} = 92.2\%$

Fig. 9: Correlation residual maps for test E3. The residuals are expressed in % of the dynamic range of the reference pictures. The arrows indicate the location of propagating cracks, whereas the white circle outlines the change in brightness as a result of limited buckling

3.6 Test E4

Figure 5(d) shows the loading history of test E4. This test consisted of 8 loading/unloading cycles. The 10-mm thick supports were utilized in addition to a relaxed connection between the MAF and the testing machine since it allowed buckling of the sample to be avoided. Observing the final deformed shape (Figure 5(c)), it was concluded that the sample remained

flat throughout the whole experiment. This observation was an additional validation of the usefulness of the anti-buckling device used herein.

Figure 10 displays measured out-of-plane displacement fields for test E4. Since the same configuration (*i.e.,* PMMA supports and relaxed connection between the MAF and the testing machine) was employed in tests E3 and E4, it was expected (and confirmed) that no notable out-of-plane displacements occurred. Furthermore, the displacement levels in elasticity (Figure 10(a)) and early plasticity (Figure 10(b)) were very small as was the case in test E3. Moreover, negligible out-of-plane displacement amplitudes were observed in the whole experiment. However, as was also the case for test E3, the sample had a tendency toward buckling, which was prevented thanks to the additional supports. This phenomenon led to non-uniform distributions of out-of-plane displacements (Figures 10(c-f)).

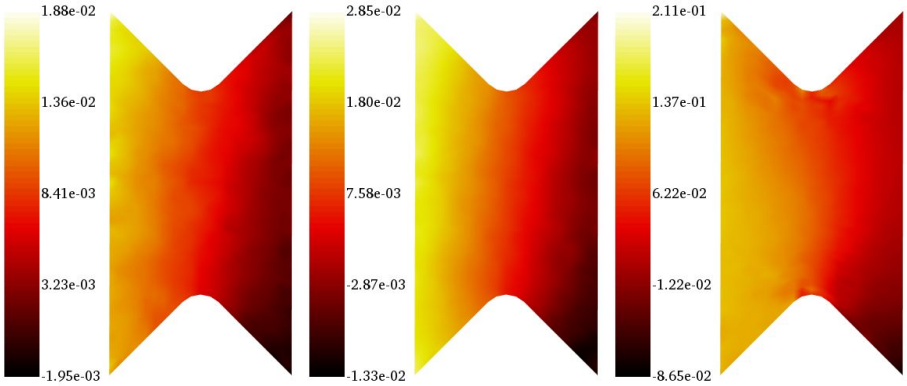

(a) $F = 4.83\text{kN}, \epsilon_{xz} = 0.25\%$ **(b)** $F = 5.44\text{kN}, \epsilon_{xz} = 0.3\%$ **(c)** $F = 8\text{kN}, \epsilon_{xz} = 26.5\%$

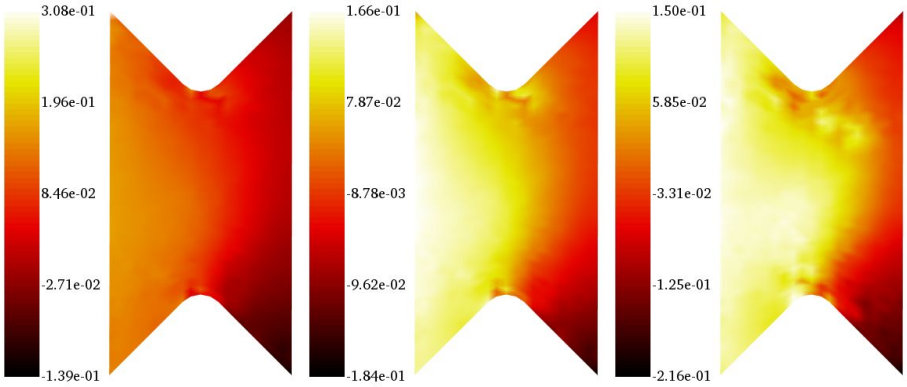

(d) $F = 8.55\text{kN}, \epsilon_{xz} = 39.8\%$ **(e)** $F = 8.65\text{kN}, \epsilon_{xz} = 47.4\%$ **(f)** $F = 8\text{kN}, \epsilon_{xz} = 68.1\%$

Fig. 10: Measured out-of-plane displacement fields for test E4. The displacements are expressed in mm

The measured axial displacement fields revealed the rotation of the ROI (Figure 11). Such rotation was also observed for test E3. Furthermore, the levels of axial displacements achieved in this test (Figure 11(a-b)) were comparable to those of test E3. Additionally, "discontinuities" arose at the roots of both V notches (Figure 11(c)). However, compared to test E3, the present discontinuities were of different sizes, which will be discussed in the sequel.

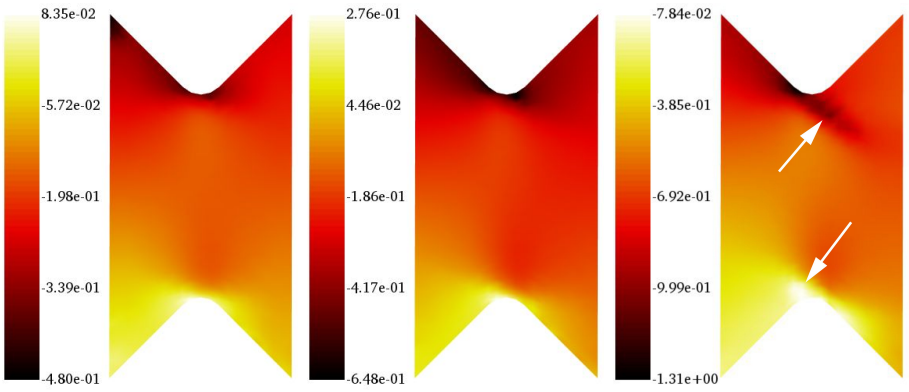

(a) $F = 8\text{kN}, \epsilon_{xz} = 26.5\%$ **(b)** $F = 8.65\text{kN}, \epsilon_{xz} = 47.4\%$ **(c)** $F = 8\text{kN}, \epsilon_{xz} = 68.1\%$

Fig. 11: Measured axial displacements for test E4. The arrows indicate the locations of the cracks. The displacements are expressed in mm

Figure 12 shows the measured shear strain fields. The shear strains were uniformly distributed at the peaks of the second and third cycles (Figure 12(a-b)). A strained band subsequently developed between the V-notches (Figures 12(c-e)) as in the previous tests. For approximately equal loads, the strain levels achieved for test E4 (Figure 12(c)) were comparable to those of tests E3 (Figure 8(c)) and E2 (Figure 22(d)), further substantiating that no buckling occurred at that point. The "discontinuity" observed in Figure 12(f) corresponded to the same phenomenon shown in Figures 11(c) and Figure 13(c), namely, the location of propagating cracks. Moreover, values for approximately equal loads (*i.e.,* 8 kN) for tests E4 (Figure 12(f)) and E3 (Figure 12(e)) were comparable.

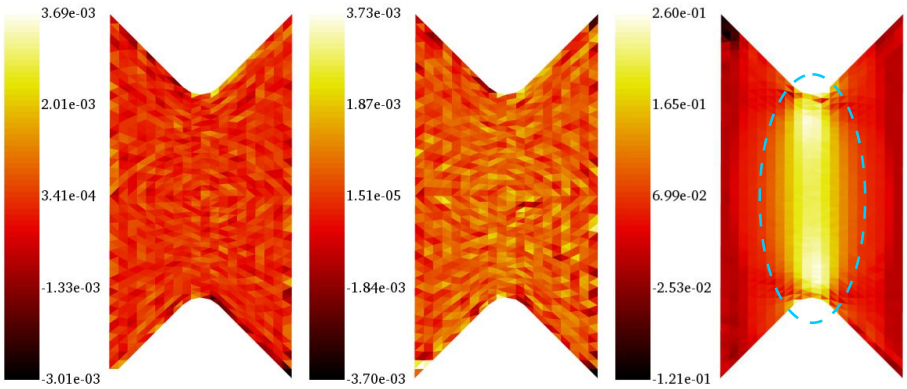

(a) $F = 4.83\text{kN}, \epsilon_{xz} = 0.25\%$ **(b)** $F = 5.44\text{kN}, \epsilon_{xz} = 0.3\%$ **(c)** $F = 8\text{kN}, \epsilon_{xz} = 26.5\%$

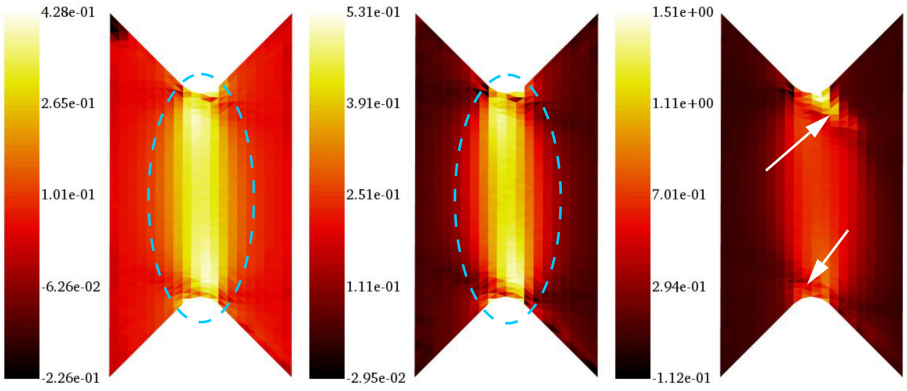

(d) $F = 8.55\text{kN}, \epsilon_{xz} = 39.8\%$ **(e)** $F = 8.65\text{kN}, \epsilon_{xz} = 47.4\%$ **(f)** $F = 8\text{kN}, \epsilon_{xz} = 68.1\%$

Fig. 12: Measured ϵ_{xz} strain fields for test E4. The strained band is outlined by blue ellipses, whereas the location of strain discontinuities (*i.e.,* cracks) are indicated by arrows

The rises in correlation residuals observed in Figure 13(a-b)) were attributed to speckle pattern smearing due to the motion of the PMMA supports with respect to the sample surface. Furthermore, the increase in correlation residuals on the edges of the ROI were attributed to speckle pattern smearing due to overly tightened PMMA plates. Since the sample exhibited a tendency toward buckling, the central part of the plates was subjected to bending thus increasing the contact pressure on the edges of the sample. For test E3, two cracks initi-

ated approximately at the same time and propagated symmetrically (Figure 9(c)). However, for test E4, the crack located at the top V-notch (Figure 13(c)) initiated earlier than that at the lower V-notch thus propagating farther.

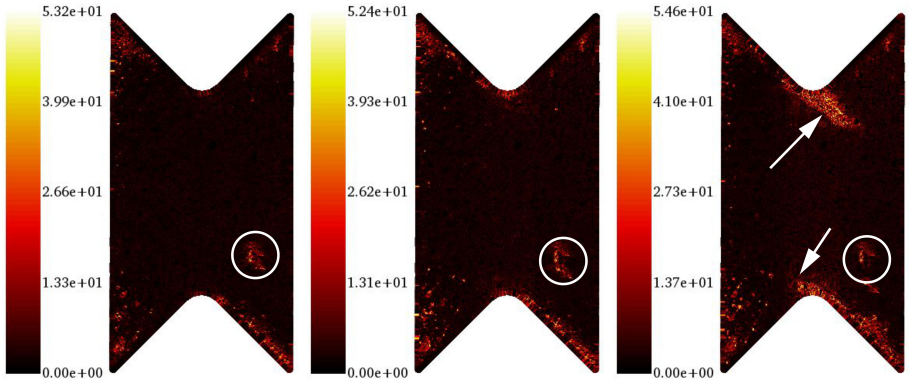

(a) $F = 8\text{kN}, \epsilon_{xz} = 26.5\%$ **(b)** $F = 8.65\text{kN}, \epsilon_{xz} = 47.4\%$ **(c)** $F = 8\text{kN}, \epsilon_{xz} = 68.1\%$

Fig. 13: Correlation residual maps for test E4. The residuals are expressed in % of the dynamic range of the reference pictures. The arrows indicate the location of propagating cracks. The white circles outline smearing of the speckle pattern on the surface due to relative motions of the sample surface with respect to the PMMA supports

3.7 Discussion

In this section, the global response is compared for each test presented in the previous sections. In order to calculate the engineering stress, the measured force for each experiment was divided by the initial cross-sectional area S_0 between the V notches of the corresponding sample. The respective stress-strain curves are shown in Figure 14.

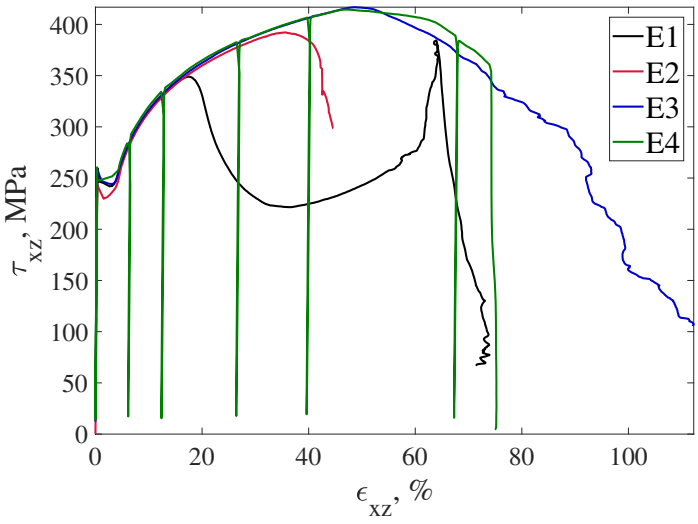

Fig. 14: Macroscopic stress/strain responses of the four analyzed tests

A good agreement in terms of global response is observed until instability inception due to buckling. Test E1 was stable up to 17% shear strain, which was proven by the measured out-of-plane displacement fields reported in Figure 19. Until this critical state, the magnitude of out-of-plane displacements was low. Since buckling occurred in test E1, additional supports were applied in test E2. A good reproducibility is observed for the global response between tests E2, E3 and E4 up to 34% shear strain. The instability in test E2 was due to the large level of preload (*i.e.,* the connection between the MAF and the test machine was very stiff). No instability was observed for tests E3 and E4 (*i.e.,* no buckling was noted when the connection between the MAF and the test machine was loosened and thicker supports were utilized). Furthermore, the agreement between tests E3 and E4 further validated the proposed setup for cyclic loadings.

Table 4 gathers characteristic values for each experiment. Similar yield stresses were observed regardless of the employed configuration. It was concluded that instability initiated

in the plastic regime. Furthermore, the highest ultimate load was achieved in tests E3 and E4 for a corresponding shear strain of 48%, and an ultimate shear strength of 417 MPa. A good reproducibility between the reported quantities for tests E3 and E4 was noted, which fully validated the third configuration. With the application of the PMMA plates onto sample E2, buckling was delayed, thereby leading to a 43 MPa higher ultimate shear strength compared to test E1. With thicker supports and loosened connection, the ultimate strength further increased by 25 MPa compared to test E2. The resulting shear strains at the ultimate load are 10-30% higher for tests E3 and E4 compared to tests E2 and E1, respectively.

Table 4: Characteristic values for the four shear tests on the Modified Arcan Fixture

Test	Yield stress, MPa	Ultimate shear strength, MPa	Ultimate load, kN	Shear strain at ultimate load, %
E1	259	349	7.3	17.5
E2	243	392	8.2	35.6
E3	258	417	8.71	48.7
E4	261	417	8.66	47.4

4 Analysis of friction between PMMA plates and the sample

In this section, the influence of friction between the PMMA plates and the sample surfaces is reviewed and discussed. It was assumed that the effect of friction was small since all experiments displayed identical responses before buckling occurred (Figure 5). Further, the speckle pattern did not degrade too much since sterecorrelation could be run until the end of each test. During the installation of the PMMA supports, the six M6 bolts were not tightened in order to minimize friction and contact pressure between the sample surface and the plates. In the following, a numerical study is presented for more quantitative evaluations of the effect of friction.

4.1 Parameter calibration

In order to numerically describe the material behavior during mechanical tests, reliable parameters are needed. FEMU was employed to calibrate the sought parameters for test E3. The material model used in the identification procedure was implemented in the commercial software *Abaqus*. Nonlinear kinematic hardening follows Armstrong-Frederick's model [38]. Thus, the sought parameters were the yield stress σ_y, hardening modulus C, and nonlinear coefficient c.

Within FEMU frameworks, differences between measured and computed quantities are minimized by iteratively updating the material parameters based on sensitivity fields [39]. If only the measured displacement fields are considered (*i.e.,* FEMU-U), the cost function is expressed as the squared error between measured $\{\mathbf{u}_m\}$ and computed $\{\mathbf{u}_c\}$ nodal displacements

$$\chi_u^2(\{\mathbf{p}\}) = \frac{1}{\gamma_u^2 N_u} \left\| \{\mathbf{u}_m\} - \{\mathbf{u}_c\} \right\|^2, \tag{1}$$

where $\{\mathbf{p}\}$ is the column vector gathering all unknown material parameters, γ_u the standard displacement uncertainty, and N_u the number of kinematic degrees of freedom [40]. With such setting, χ_u tends to 1 when the only source of error is due to measurement uncertainty. Any deviation from 1 is an indication of model error.

The identification procedure can also be conducted with respect to measured loads $\{\mathbf{F}_m\}$ and computed reaction forces $\{\mathbf{F}_c\}$ (FEMU-F) extracted from edges where Dirichlet boundary conditions are prescribed

$$\chi_F^2(\{\mathbf{p}\}) = \frac{1}{\gamma_F^2 N_F} \left\| \{\mathbf{F}_m\} - \{\mathbf{F}_c\} \right\|^2, \tag{2}$$

where γ_F is the standard uncertainty of the load cell, and N_F the number of load data.

The combination of the aforementioned cost functions (*i.e.,* FEMU-UF) is expressed as

$$\chi^2_{tot} = (1-\omega)\chi^2_u + \omega\chi^2_F, \tag{3}$$

where the parameter ω determines the contribution of each individual cost function. For the present study, the latter was set to $\omega = 0.5$, which endowed each cost function with equal weight.

The FE mesh used in the identification procedure was constructed from the measurement mesh (Figure 4). It was converted into four-noded quadrilateral (Q4) elements, and then extruded to obtain C3D8 elements with reduced integration (C3D8R). The measured displacements were prescribed along the stressed edges of the mesh as Dirichlet boundary conditions (Figure 16(a)). The elastic parameters (*i.e.,* Young's modulus E and Poisson's ratio ν) were kept constant and equal to their nominal values (Table 5). Only the aforementioned plastic parameters were calibrated.

Table 5: Identification results via FEMU-UF

	E, GPa	ν, -	σ_{Y}, MPa	C, GPa	c, -	χ_{U}	χ_{F}
Initial	210	0.25	250	6000	15	35	116
Identified	210	0.25	365	4635	13	23	11

Once calibrated, the parameters yielded significant decreases in both displacement and force residuals (Table 5). Furthermore, the identification resulted in a very good agreement between the global reaction forces extracted from the FE model and the measured forces (Figure 15), which led to residuals that were on average only 11 times the uncertainty level. However, in elasticity, the computed response was slightly offset from the measured curve. This trend is believed to be due to the fact that the Dirichlet boundary conditions had to

be extruded. The identified material parameters reported in Table 5 were used in further numerical simulations. The calibrated value of the yield stress was higher than the expected value estimated from the *macroscopic* stress-strain curve (Figure 14). This difference was due to the fact that even in the elastic regime, the stress state was not uniform in the ligament.

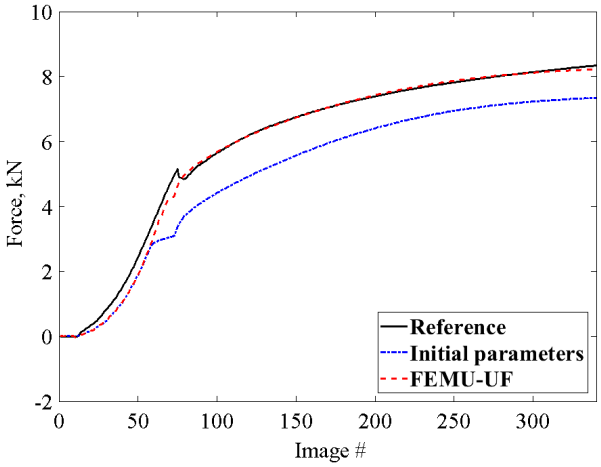

Fig. 15: Comparison between measured and resultant forces extracted from the FE model of test E3

4.2 Effect of friction

The effect of friction was studied via complete FE simulations of test E3 with the two PMMA plates. The sample was again discretized with C3D8R elements, and the PMMA plates with C3D4 tetrahedra. The boundary conditions on the model were the same as in the identification procedure. However, rigid body out-of-plane motions were eliminated. Bolts were replaced by a combination of kinematic coupling and connector elements (CONN3D2, type = beam). Bolt heads were replaced with kinematic couplings (Figure 16(b) depicted by blue lines) on the PMMA surfaces around the bolt holes, while the bolt shaft was simu-

lated with connector elements. The master nodes of the kinematic coupling were attached with the connector elements, which ensured stiff connections between nodes. Since the bolts were not pre-loaded, the bolt pretension was not simulated. All out-of-plane motions were disabled in the the master nodes of the kinematic couplings for both PMMA plates. Furthermore, for a single master node, the remaining displacements and all rotations (Figure 16(b) depicted by the red dot) were disabled to suppress the rigid body motions of the plates. The plates were assumed to remain elastic (with a 3 GPa Young's modulus and 0.3 Poisson's ratio). Between the sample and PMMA surfaces, general contact was defined with Coulomb friction [41]. Since damage initiation and growth was out of the scope of this work, the simulations were carried out only for the first 330 time steps (Figure 5(c)) of the experiment (*i.e.,* before damage occurred).

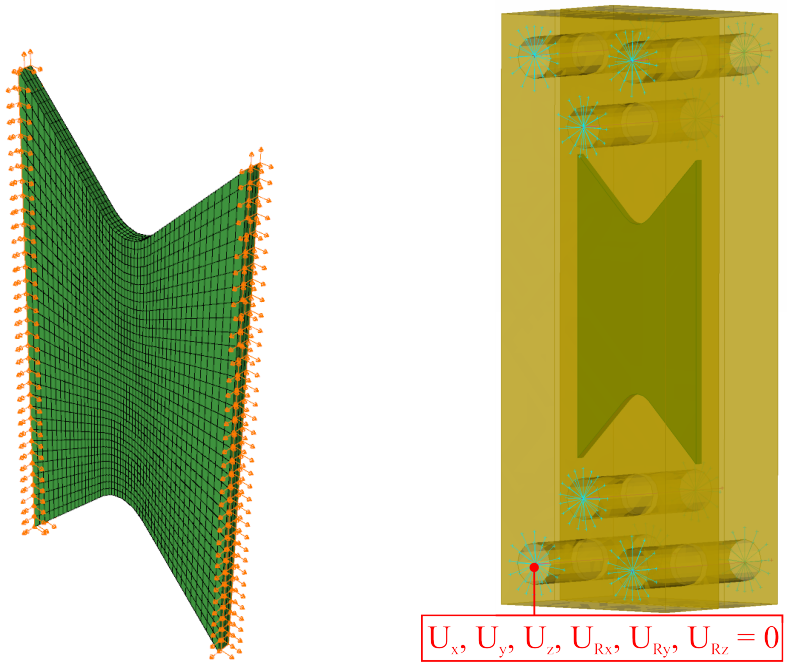

Fig. 16: FE model of test E3. (a) E3 sample with prescribed measured displacements as boundary conditions. (b) Assembly of sample E3 and PMMA plates

It was expected that the resultant forces extracted from the stressed edges of the model were sensitive to friction. In the available literature, the reported values of friction coefficient between PMMA and steel vary [42, 43, 44, 45]. However, the estimated levels generally range from 0.3 to 0.4. First, FEMU-UF was run to calibrate plastic parameters for a very low friction coefficient (*i.e.,* $\mu = 0.01$). The calibrated parameters are reported in Table 6; they were similar to those obtained previously even though the boundary conditions were different (Table 5). The calibrated material parameters were then used to initialize the second FEMU-UF analysis where, additionally, the friction coefficient was sought. The initial value was set to $\mu = 0.3$, which corresponded to the lower bound found in the surveyed

literature. The parameters calibrated along with μ all decreased (the hardening modulus C experienced the largest relative reduction). The global residual χ_{tot} (Equation (3)) only slightly decreased.

Table 6: Identification results for low friction value and calibrated material parameters and friction coefficient μ

	E, GPa	ν, -	σ_Y, MPa	C, MPa	c, -	χ_{tot}	$\delta\overline{\sigma}$, MPa
$\mu = 0.01$	210	0.25	365	4616	13.1	43	-
$\mu = 0.33$	210	0.25	357	3860	11.8	42.6	38

To further illustrate the effect of friction on the calibrated parameters, a uniaxial tensile loading was applied to a single C3D8R element. Dirichlet boundary conditions were prescribed on four surface nodes of the cube (denoted by arrows in Figure 17(a)), whereas on the opposite surface, both rigid body displacements and rotations were disabled. The prescribed displacements ranged from 0 to 0.47 times the element height with a step size of 0.001 (*i.e.,* corresponding to the strain levels obtained via the DIC virtual gauge before damage occurred). The differences between stresses for the frictionless (reference) case (*i.e.,* $\mu = 0.01$) and for the calibrated value ($\mu = 0.33$) were not monotonic with respect to the strain level. The mean stress difference $\delta\overline{\sigma}$ was equal to 38 MPa (Figure 17(b)), which indicated that friction had a non negligible effect on the calibrated kinematic hardening parameters.

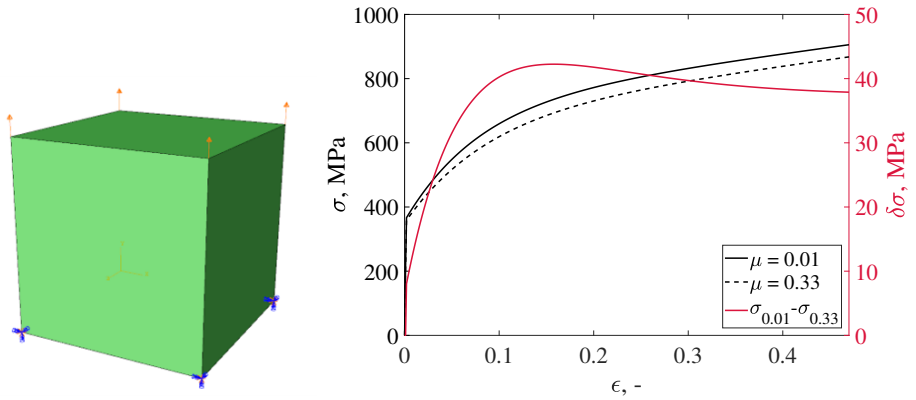

Fig. 17: (a) Cube element used for depicting the tensile response with the calibrated parameters (Table 6) and the corresponding boundary conditions. (b) Stress-strain curves calculated for $\mu = 0.01$ and $\mu = 0.33$ with the respective material parameters (black curves) and corresponding stress differences (red curve)

From the numerical simulation with the calibrated material parameters and friction coefficient, the stress triaxiality fields were evaluated. In Figure 18, the triaxiality field is displayed for the last analyzed image when $\mu = 0.33$. From the triaxiality field, it was concluded that the gauge area was predominantly subjected to shear stresses (*i.e.,* stress triaxialities close to zero). This result was observed for the central points through the thickness (*i.e.,* points 1,2 and 3), which displayed slight deviations in stress triaxialities yet close to zero. This trend was observed for all analyzed images. For the chosen points in the root of the V notch, the stress triaxiality changed significantly with the applied shear strain. For low shear strains, the stress triaxiality was closer to zero (*i.e.,* shear stress state). At the root of the V notch, complex stress states were expected, which were observed from the deviation of the middle point (*i.e.,* point 5), whereas the surface points had almost identical

levels. Moreover, the areas around the V notch where the material was subjected to tensile stresses (*i.e.,* stress triaxiality close to 0.33) corresponded to the locations of initiated cracks (Figure 5(c)).

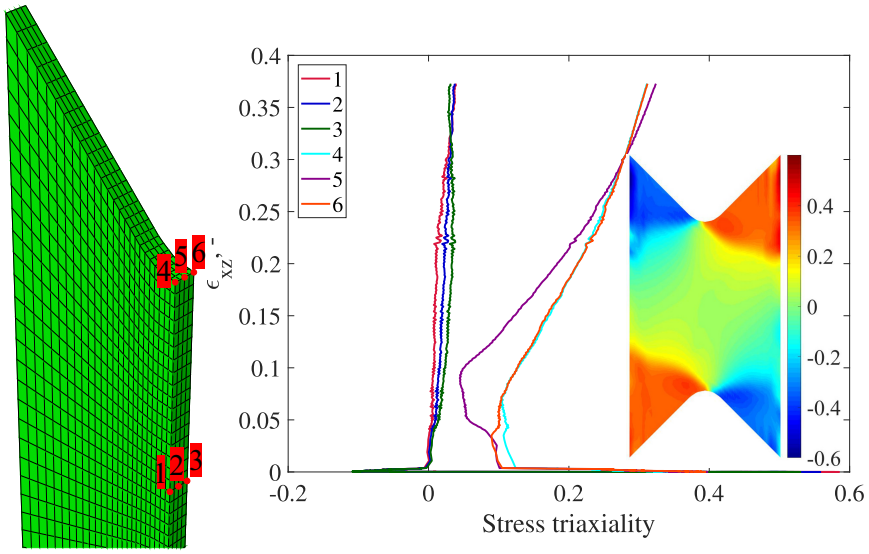

Fig. 18: Stress triaxiality history for six different points with respect to the calculated shear strain in the virtual gauge and the triaxiality field for the last computed image (*i.e.,* frame 330) when $\mu = 0.33$

5 Conclusion

The experimental campaign performed herein was aimed at preventing buckling to occur in thin (*i.e.,* 1 mm) butterfly samples under simple shear loading on a modified Arcan fixture (MAF). Three monotonic shear tests and one additional cyclic test were carried out. They were monitored with a stereovision system, and the kinematic fields were measured by means of FE-based stereocorrelation. Three different configurations of the experimental setup were studied considering anti-buckling devices and connection stiffness between the

MAF and the testing machine. Furthermore, friction between the anti-buckling device and the sample was evaluated and subsequently calibrated via FEMU-UF. The main results of this work are:

- shear buckling was successfully suppressed for Arcan butterfly samples with a large gauge area using the thickest anti-buckling device,
- FEMU using measured displacements prescribed as Dirichlet boundary conditions on the FE model was carried out to calibrate kinematic hardening parameters,
- the influence of the friction coefficient on the calibrated material parameters was studied using a numerical model of the sample and the anti-buckling device,
- the friction coefficient between the PMMA anti-buckling device and the sample surface could also be calibrated ($\mu = 0.33$).

Last, a detailed analysis of the prescribed boundary conditions on the FE model of the butterfly sample may provide optimal routes to avoid complex numerical simulations (*i.e.,* modeling of the sample and the anti-buckling device).

Acknowledgements

This work was performed within the FULLINSPECT project supported by the Croatian Science Foundation (UIP-2019-04-5460 Grant). The authors also acknowledge and thank EikoSim for providing the EikoTwin DIC software to conduct the stereocorrelation analyses reported herein.

6 Compliance with Ethical Standards

The authors have no conflict of interest to declare.

References

1. Tisza M (2005) Numerical modeling and simulation in sheet metal forming academic and industrial perspectives. Mater Sci Forum 473-474:407–414, 10.4028/www.scientific.net/MSF.473-474.407
2. Ghosh AK, Bae DG (2000) A planar simple shear test and flow behavior in a superplastic Al-Mg alloy. Metall Mater Trans 34(11):2465–2471, https://doi.org/10.1007/s11661-003-0006-3
3. Rauch EF (1998) Plastic anisotropy of sheet metals determined by simple shear tests. Mater Sci Eng A 241(1-2):179–183, https://doi.org/10.1016/S0921-5093(97)00486-3
4. Bouvier S, Haddadi H, Levée P, Teodosiu C (2006) Simple shear tests: Experimental techniques and characterization of the plastic anisotropy of rolled sheets at large strains. Journal of Materials Processing Technology 172(1):96–103, 10.1016/j.jmatprotec.2005.09.003
5. Abedini A, Noder J, Kohar CP, Butcher C (2020) Accounting for Shear Anisotropy and Material Frame Rotation on the Constitutive Characterization of Automotive Alloys using Simple Shear Tests. Mech Mater 148(April):103419, 10.1016/j.mechmat.2020.103419
6. Miyauchi K (1984) A proposal of a planar simple shear test in sheet metals. Sci Pap Inst Phys Chem Res 78(3):27–40
7. Peirs J, Verleysen P, Degrieck J (2012) Novel Technique for Static and Dynamic Shear Testing of Ti6Al4V Sheet. Exp Mech 52(7):729–741, 10.1007/s11340-011-9541-9
8. Roth CC, Mohr D (2016) Ductile fracture experiments with locally proportional loading histories. Int J Plast 79:328–354, 10.1016/j.ijplas.2015.08.004

9. ASTM (2005) ASTM B831-05, Standard Test Method for Shear Testing of Thin Aluminum Alloy Products, ASTM International, West Conshohocken, PA, 2005, https://doi.org/10.1520/B0831-05
10. Merklein M, Biasutti M (2011) Forward and reverse simple shear test experiments for material modeling in forming simulations. Special Edition: 10th International Conference on Technology of Plasticity, ICTP 2011 pp 702–707
11. Yin Q, Zillmann B, Suttner S, Gerstein G, Biasutti M, Tekkaya AE, Wagner MFX, Merklein M, Schaper M, Halle T, Brosius A (2014) An experimental and numerical investigation of different shear test configurations for sheet metal characterization. Int J Solids Struct 51(5):1066–1074, https://doi.org/10.1016/j.ijsolstr.2013.12.006
12. Bao Y, Wierzbicki T (2004) A comparative study on various ductile crack formation criteria. Journal of Engineering Materials and Technology, Transactions of the ASME 126(3):314–324, 10.1115/1.1755244
13. Reyes A, Eriksson M, Lademo OG, Hopperstad OS, Langseth M (2009) Assessment of yield and fracture criteria using shear and bending tests. Mater Des 30(3):596–608, 10.1016/j.matdes.2008.05.045
14. Roth CC, Mohr D (2018) Determining the strain to fracture for simple shear for a wide range of sheet metals. Int J Mech Sci 149:224–240, 10.1016/j.ijmecsci.2018.10.007
15. Roth CC, Mohr D (2015) Experimental investigation on shear fracture at high strain rates. EPJ Web Conf 94:3–6, 10.1051/epjconf/20159401078
16. Iosipescu N (1967) New Accurate Procedure for Single Shear Testing of Metals. J Mater 2(3):537–566
17. Mohr D, Henn S (2007) Calibration of stress-triaxiality dependent crack formation criteria: A new hybrid experimental-numerical method. Exp Mech 47(6):805–820, 10.1007/s11340-007-9039-7

18. Mohr D, Oswald M (2008) A new experimental technique for the multi-axial testing of advanced high strength steel sheets. Exp Mech 48(1):65–77, 10.1007/s11340-007-9053-9
19. Mohr D, Doyoyo M (2003) A new method for the biaxial testing of cellular solids. Exp Mech 43(2):173–182, https://doi.org/10.1007/BF02410498
20. Arcan M, Hashin Z, Voloshin A (1978) A method to produce uniform plane-stress states with applications to fiber-reinforced materials. Exp Mech 18(4):141–146, https://doi.org/10.1007/BF02324146
21. Dunand M, Mohr D (2011) Optimized butterfly specimen for the fracture testing of sheet materials under combined normal and shear loading. Eng Fract Mech 78(17):2919–2934, 10.1016/j.engfracmech.2011.08.008
22. Abedini A, Butcher C, Anderson D, Worswick M, Skszek T (2015) Fracture Characterization of Automotive Alloys in Shear Loading. SAE Int J Mater Manuf 8(3), 10.4271/2015-01-0528
23. Abedini A, Butcher C, Worswick MJ (2017) Fracture Characterization of Rolled Sheet Alloys in Shear Loading: Studies of Specimen Geometry, Anisotropy, and Rate Sensitivity. Exp Mech 57(1):75–88, 10.1007/s11340-016-0211-9
24. Peshekhodov I, Jiang S, Vucetic M, Bouguecha A, Berhens BA (2016) Experimental-numerical evaluation of a new butterfly specimen for fracture characterisation of AHSS in a wide range of stress states. IOP Conference Series: Materials Science and Engineering 159(1), 10.1088/1757-899X/159/1/012015
25. Boni S, G'Sell C, Weynant E, Haudin JM (1982) Microscopic in situ observation of the plastic deformation of polybutene-1 films under simple shear. Polym Test 3(1):3–24, https://doi.org/10.1016/0142-9418(82)90009-5

26. Pucillo GP, Grasso M, Penta F, Pinto P (2011) On the mechanical characterization of materials by Arcan-type specimens. Eng Fract Mech 78(8):1729–1741, https://doi.org/10.1016/j.engfracmech.2011.02.002
27. Grédiac M, Hild F (eds) (2012) Full-Field Measurements and Identification in Solid Mechanics. ISTE / Wiley, London (UK)
28. Pham CH, Adzima F, Coer J, Manach PY (2017) Anti-Buckling Device for Ultra-Thin Metallic Sheets Under Large and Reversed Shear Strain Paths. Exp Mech 57(4):593–602, https://doi.org/10.1007/s11340-017-0256-4
29. Bertin M, Hild F, Roux S (2017) On the identifiability of the Hill-1948 model with one uniaxial tensile test. Comptes Rendus Mécanique 345(6):363–369, https://doi.org/10.1016/j.crme.2017.04.001
30. Bertin M, Hild F, Roux S (2017) On the identifiability of Hill-1948 plasticity model with a single biaxial test on very thin sheet. Strain 53(5):e12233, https://doi.org/10.1111/str.12233
31. Dufour J, Beaubier B, Roux S, Hild F (2014) Displacement measurement using CAD-based stereo-correlation with meshes. In: ICEM conference, 10.1007/978-3-319-06986-9_34
32. Dubreuil L, Dufour JE, Quinsat Y, Hild F (2016) Mesh-based shape measurements with stereocorrelation. Experimental Mechanics 56(7):1231–1242, https://doi.org/10.1007/s11340-016-0158-x
33. Pierré JE, Passieux JC, Périé JN (2017) Finite Element Stereo Digital Image Correlation: Framework and Mechanical Regularization. Experimental Mechanics 57(3):443–456, https://doi.org/10.1007/s11340-016-0246-y
34. EikoSim Company (2020) EikoTwin DIC. https://eikosim.com/en/eikotwin-2/

35. Beaubier B, Dufour J, Hild F, Roux S, Lavernhe-Taillard S, Lavernhe-Taillard K (2014) CAD-based calibration of a 3D-DIC system: Principle and application on test and industrial parts. Experimental Mechanics 54(3):329–341, 10.1007/978-1-4614-4235-6_32
36. Dufour JE, Beaubier B, Hild F, Roux S (2015) CAD-based displacement measurements. Principle and first validations. Experimental Mechanics 55(9):1657–1668, https://doi.org/10.1007/s11340-015-0065-6
37. Hild F, Bouterf A, Roux S (2015) Damage Measurements via DIC. International Journal of Fracture 191(1-2):77–105, 10.1007/s10704-015-0004-7
38. Armstrong P, Frederick C (1966) A mathematical representation of the multiaxial bauschinger effect. CEGB Rep RD/B/N660
39. Tarantola A (1987) Inverse Problems Theory. Methods for Data Fitting and Model Parameter Estimation. Elsevier Applied Science, Southampton (UK)
40. Mathieu F, Leclerc H, Hild F, Roux S (2015) Estimation of elastoplastic parameters via weighted FEMU and integrated-DIC. Experimental Mechanics 55(1):105–119
41. Coulomb C (1821) Theorie des machines simples (in French). Bachelier, Paris (France)
42. Rabbe LM, Rieu J, Lopez A, Combrade P (1994) Fretting deterioration of orthopaedic implant materials: Search for solutions. Clin Mater 15:221–226, 10.1016/0267-6605(94)90049-3
43. Nuño N, Amabili M, Groppetti R, Rossi A (2001) Static coefficient of friction between Ti-6A1-4V and PMMA for cemented hip and knee implants. J Biomed Mater Res 59(1):191–200, 10.1002/jbm.1233
44. Lim A, Castagne S, Wong CC (2014) Effect of Friction Coefficient on Finite Element Modeling of the Deep - Cold Rolling Process. In: Int. Conf. Shot Peen., pp 376–380
45. Nuño N, Groppetti R, Senin N (2006) Static coefficient of friction between stainless steel and PMMA used in cemented hip and knee implants. Clin Biomech 21(9):956–

962, 10.1016/j.clinbiomech.2006.05.008

Appendix A

This appendix gathers stereocorrelation results of tests E1 and E2 that enabled for the improvements utilized in tests E3 and E4.

6.1 Test E1

Figure 19 shows out-of-plane displacement fields for different load levels (Figure 5(a)) and strain values. Positive displacements are oriented away from the reader. Low out-of-plane displacements were measured in the elastic regime of the sample (Figure 19(a)). Furthermore, the inception of plasticity (Figure 19(b)) was also characterized by small out-of-plane displacements. However, for the 7.2-kN load level (*i.e.,* the first peak on the load-time plot of Figure 5), the out-of-plane displacement amplitudes increased. This growing trend continued while further loading the sample. Furthermore, the out-of-plane displacement distribution was symmetric, which was also observed on the deformed sample in Figure 5(a). The aforementioned symmetry was observed in the displacement levels (*i.e.,* displacement amplitudes were similar in Figure 19(d-f)). Even though a stereovision system was employed, these high levels of measured displacement were not considered reliable since the out-of-plane rotation of the ROI caused some parts to be out of focus.

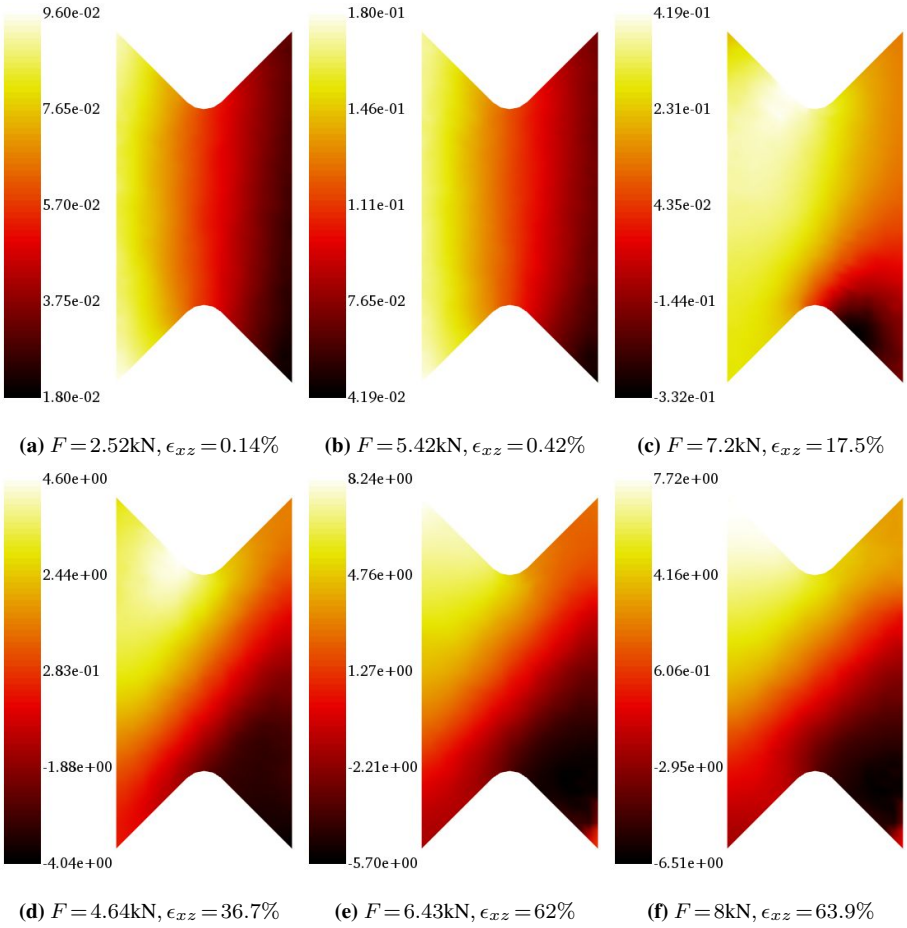

(a) $F = 2.52\text{kN}, \epsilon_{xz} = 0.14\%$ **(b)** $F = 5.42\text{kN}, \epsilon_{xz} = 0.42\%$ **(c)** $F = 7.2\text{kN}, \epsilon_{xz} = 17.5\%$

(d) $F = 4.64\text{kN}, \epsilon_{xz} = 36.7\%$ **(e)** $F = 6.43\text{kN}, \epsilon_{xz} = 62\%$ **(f)** $F = 8\text{kN}, \epsilon_{xz} = 63.9\%$

Fig. 19: Measured out-of-plane displacement fields for test E1. The displacements are expressed in mm. F denotes the applied load, and ϵ_{xz} the average shear strain calculated with the optical gauge

Figure 20 shows measured shear strain fields for different load levels (Figure 5(a)). The average strain levels in elasticity (Figure 20(a)) and at the inception of plasticity (Figure 20(b)) were low as expected. Furthermore, a single strained band developed between the V notches where the strain levels were one order of magnitude higher than on the edges of

the ROI (Figure 20(c)). The rotation of the ROI due to buckling is observed in Figure 20(d). Further measurements (Figure 20(e-f)) were deemed unreliable.

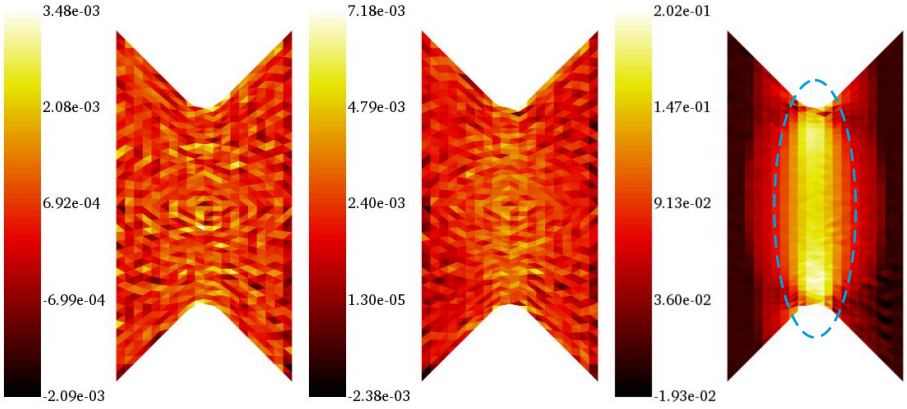

(a) $F = 2.52\text{kN}, \epsilon_{xz} = 0.14\%$ **(b)** $F = 5.42\text{kN}, \epsilon_{xz} = 0.42\%$ **(c)** $F = 7.2\text{kN}, \epsilon_{xz} = 17.5\%$

(d) $F = 4.64\text{kN}, \epsilon_{xz} = 36.7\%$ **(e)** $F = 6.43\text{kN}, \epsilon_{xz} = 62\%$ **(f)** $F = 8\text{kN}, \epsilon_{xz} = 63.9\%$

Fig. 20: Measured ϵ_{xz} strain fields for test E1. F denotes the applied load, and ϵ_{xz} the average shear strain calculated via the virtual sensor. The strained band is outlined by a dashed blue ellipse

Test E2

Figure 21 shows measured out-of-plane displacements for characteristic load levels (Figure 5(b)) and strain values. As for test E1, the out-of-plane displacements were very small in the elastic regime (Figure 21(a)) as well as for a large part of the plastic regime (Figure 21(b-d)). However, clear signs of buckling initiation were observed (Figure 21(e-f)). The displacements in the center of the sample were negative, whereas on the opposite corners they were positive. This result indicated that wrinkling had started, and was also observed from the shape of the deformed sample in (Figure 5(b)). The PMMA support fractured due to increased buckling. Thus, stereocorrelation results were no longer deemed reliable beyond this point.

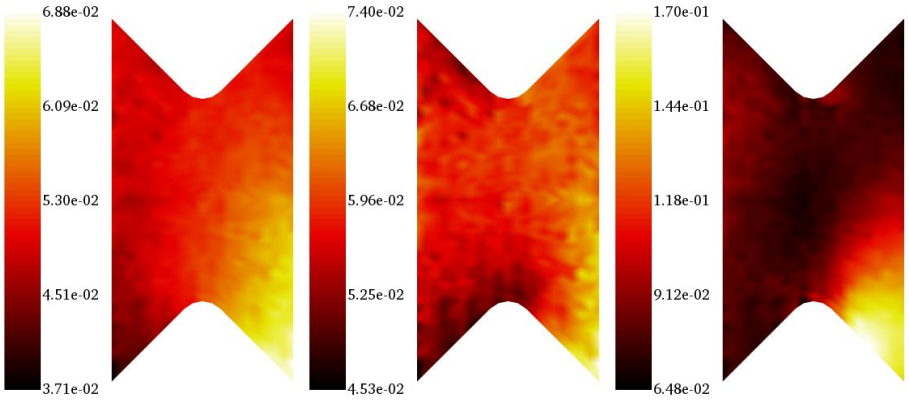

(a) $F = 1.94$kN, $\epsilon_{xz} = 0.09\%$ **(b)** $F = 5$kN, $\epsilon_{xz} = 0.34\%$ **(c)** $F = 6.7$kN, $\epsilon_{xz} = 11\%$

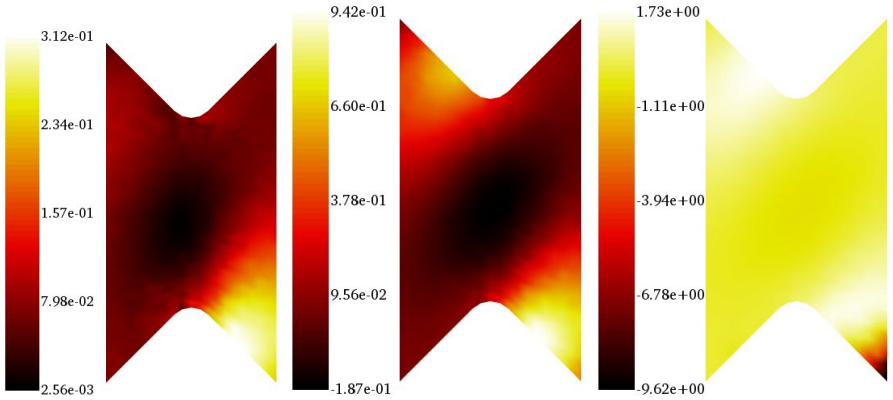

(d) $F = 7.6$kN, $\epsilon_{xz} = 22\%$ **(e)** $F = 8.2$kN, $\epsilon_{xz} = 35.5\%$ **(f)** $F = 7.85$kN, $\epsilon_{xz} = 41.4\%$

Fig. 21: Measured out-of-plane displacement fields for test E2. The displacements are expressed in mm

Figure 22 displays measured shear strain fields. Since buckling of the sample was delayed, the material response (*i.e.,* strain fields) was captured more reliably. Since only elastic strains were present in Figure 22(a-b), they were rather evenly distributed over the ROI, and were at least one order of magnitude higher than the noise floor levels (Table 3). Furthermore, a single strained band developed between the two V notches (Figure 22(c)) and was observed until the end of the test (Figure 22(d-e)). Comparing strains between tests E2 and

E1, higher levels were achieved due to the more stable material response thanks to the additional supports.

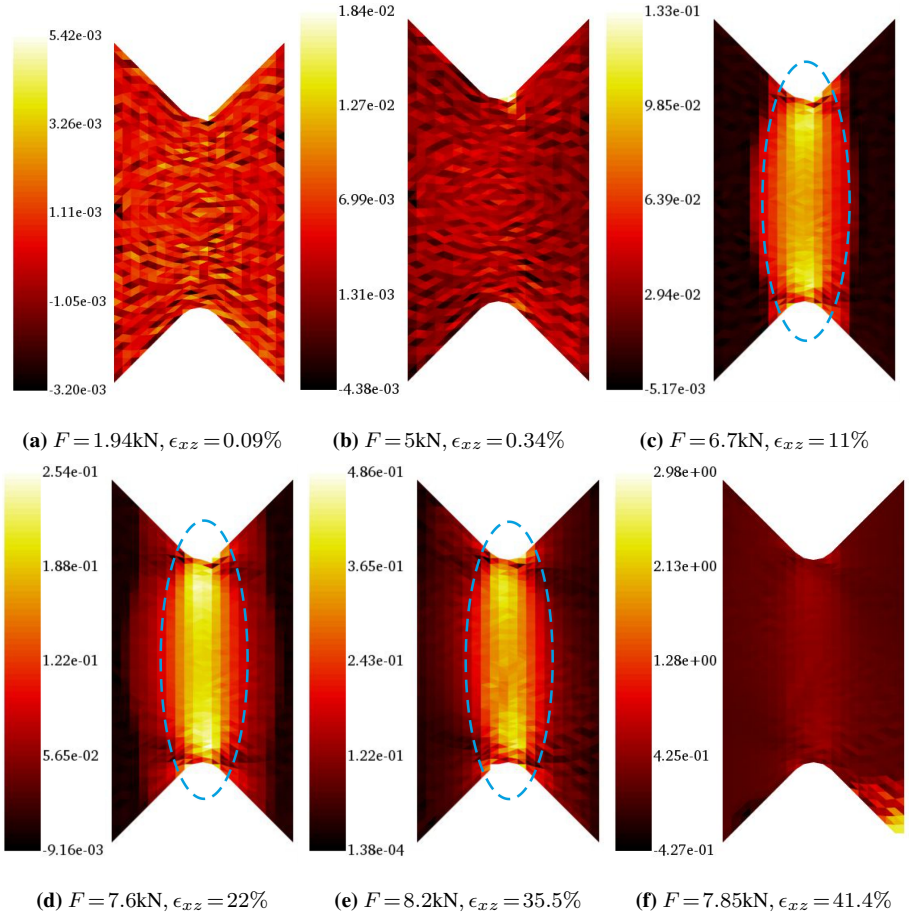

(a) $F = 1.94\text{kN}, \epsilon_{xz} = 0.09\%$ **(b)** $F = 5\text{kN}, \epsilon_{xz} = 0.34\%$ **(c)** $F = 6.7\text{kN}, \epsilon_{xz} = 11\%$

(d) $F = 7.6\text{kN}, \epsilon_{xz} = 22\%$ **(e)** $F = 8.2\text{kN}, \epsilon_{xz} = 35.5\%$ **(f)** $F = 7.85\text{kN}, \epsilon_{xz} = 41.4\%$

Fig. 22: Measured ϵ_{xz} strain fields for test E2. The strained band is outlined by dashed blue ellipses